International Journal of Plasticity 149 (2022) 103157

Contents lists available at ScienceDirect

International Journal of Plasticity

journal homepage: www.elsevier.com/locate/ijplas

Atomistic simulations of the local slip resistances in four refractory multi-principal element alloys

Rebecca A. Romero [a,b], Shuozhi Xu [c,*], Wu-Rong Jian [c], Irene J. Beyerlein [c,d], C. V. Ramana [b,e]

[a] Department of Metallurgical, Materials and Biomedical Engineering, The University of Texas at El Paso, El Paso, TX 79968, USA
[b] Center for Advanced Materials Research, The University of Texas at El Paso, El Paso, TX 79968, USA
[c] Department of Mechanical Engineering, University of California, Santa Barbara, CA 93106-5070, USA
[d] Materials Department, University of California, Santa Barbara, CA 93106-5050, USA
[e] Department of Mechanical Engineering, The University of Texas at El Paso, El Paso, TX 79968, USA

ARTICLE INFO

Keywords:
Multi-principal element alloys
Dislocations
Local slip resistances
Lattice distortion

ABSTRACT

The design and development of structural materials that can survive under the extreme conditions of operation are critical to next generation aerospace and energy technologies. Selectively designed multi-principal element alloys (MPEAs), which are solid solution phases with three or more principal elements on simple underlying lattices, are expected to fulfill such requirements. The combination of refractory metals with elements known for enhancing oxidation resistance, high temperature strength, and thermal stability makes them ideal candidates for high temperature applications. Due to their unique microstructures and chemical compositions, MPEAs may exhibit excellent mechanical properties, such as high strengths at elevated temperatures and improved hardnesses. Improving the mechanical properties of MPEAs requires knowledge of their plastic deformation mechanisms, at the core of which is dislocation slip, which is intimately connected to the local slip resistances (LSRs). In this work, atomistic calculations are conducted to obtain LSRs of edge and screw dislocations on three slip planes – {110}, {112}, and {123} – in four refractory MPEAs, CrMoNbTa, CrNbTaW, MoNbTaV, and MoNbTaW.The goal of this work is to determine the LSR and the role that lattice distortion has. We find that the two MPEAs containing Cr bear an increased lattice distortion and achieve the highest LSR values and lowest anisotropy in LSR. It is also shown that the MPEAs possess much lower slip resistance anisotropy than pure metals.

1. Introduction

The need for structural materials that can withstand extreme conditions, such as high temperatures, continue to push efforts for designing and developing such materials. Conventional alloy families focus on utilizing one main constituent element with small amounts of additional elements to enhance material properties. Unlike conventional alloys, multi-principal element alloys (MPEAs) employ the approach of using multiple elements in equiatomic or near-equiatomic proportion. This concept was first proposed by Yeh et al. (2004) and Cantor et al. (2004). These equiatomic alloys formed stable solid solutions, which was attributed to their high

* Corresponding author.
E-mail address: shuozhixu@ucsb.edu (S. Xu).

https://doi.org/10.1016/j.ijplas.2021.103157
Received 15 July 2021; Received in revised form 16 November 2021;
Available online 30 November 2021

configurational entropies of mixing. Both studies found an absence of complex phases and microstructures, which encouraged the further development of other MPEAs.

The theory of incorporating refractory metals into such alloys was later applied in Mo-Nb-Ta-W and Mo-Nb-Ta-V-W alloys (Senkov et al., 2010). The idea was to create alloys suitable for use in applications that require high strength at high operating temperatures, such as those in the aerospace and energy industries. The combination of high melting temperature and creep resistance, specifically in the temperature range of 830–1830 °C, make refractory metals good candidate materials for high temperature applications (Wadsworth et al., 1988). Senkov et al. (2011) produced two equiatomic alloy compositions ($Mo_{25}Nb_{25}Ta_{25}W_{25}$ and $Mo_{20}Nb_{20}Ta_{20}V_{20}W_{20}$) based on refractory elements. These MPEAs were found to have good plastic flow and compressive strain. The strength and resistance to softening were attributed to a slow diffusion of elements at high temperatures and retention of a dendritic microstructure. The same study also showed a promising compressive yield strength at elevated temperatures. When compared to Inconel 718 and Haynes 230, both MPEAs had a normalized yield stress two to four times higher at 1000 °C. The encouraging results of these studies prompted further exploration into the strength, specifically at elevated temperatures, of MPEAs using refractory elements. A comprehensive review of mechanical data of these alloys can be found in the work of Couzinié et al. (2018).

The potential identified in the refractory group of alloys sparked further investigation into refractory MPEAs containing Mo, Nb, Ta, V, and W. MoNbTaVW was fabricated through mechanical alloying and spark plasma sintering (Kang et al., 2018). Using this fabrication process, the alloy was able to obtain a compressive yield strength of 2612 MPa at room temperature, nearly doubling that of the same alloy fabricated through vacuum arc melting found by Senkov et al. (2011). This demonstrates the ability for the alloy properties to be enhanced through processing and further proves the high strength potential this class of alloys may possess. Other variations of this alloy family have been studied, for which the mechanical properties of the alloy obtained either a higher hardness or compressive yield strength than the individual constituent elements (Zhang et al., 2015; Han et al., 2018; Xiao et al., 2019; Yao et al., 2016a; Waseem et al., 2018). In MPEAs containing Cr (*e.g.*, Cr_xMoNbTaVW, CrMoNbTaV, and CrTaTi_xVW), the mechanical properties were enhanced due to the lattice distortion caused by Cr's smaller atomic radius (Zhang et al., 2015; Xiao et al., 2019; Waseem et al., 2018).

One of the biggest drawbacks of using refractory metallic alloys is their poor high temperature oxidation resistance. MPEAs present an opportunity to provide an improved oxidation resistance by way of high concentrations of alloying elements beneficial for oxidation resistance. A major aspect of the work done on refractory MPEAs has revolved around combining elements with high melting points known for having high temperature strength and thermal stability (*e.g.*, Hf, Mo, Nb, Ta, W, and Zr) with elements beneficial for oxidation resistance (*e.g.*, Al, Cr, Ti, and Si) (Senkov et al., 2018). Of the 20 compiled refractory MPEA oxidation studies reported, 14 contained Cr, an essential element advantageous for improving oxidation behavior. Cr is commonly used in stainless steel and Ni-based superalloys for its ability to form a passivating layer and its relatively low density. The importance of Cr can be seen in the refractory MPEAs containing Al, Si, Ti, Nb, Mo, and Ta. An $Al_{17}Si_3Ti_5Cr_{25}Nb_{15}Mo_{20}Ta_{15}$ alloy was evaluated at 1000 and 1100 °C for 200 h of oxidation by Lo et al. (2019). This oxidation exposure time is significantly longer than other oxidation studies. It was reported that the formation of $CrTaO_4$ protected the alloy from catastrophic oxidation by hindering the outward diffusion of refractory elements. The formation of other Cr-containing oxides ($CrNbO_4$ and Cr_2O_3) demonstrated a positive effect on the oxidation behavior of both Nb-based alloys and refractory MPEAs (Chan, 2004; Gorr et al., 2016).

The many encouraging results obtained from these studies emboldens the potential for further studies of these alloys. The difficulty comes in processing and fabricating these alloys, as they can be time consuming and expensive. On the other hand, atomistic calculations can provide insight into various alloy compositions and help predict the plastic deformation behavior. Numerical studies of the plastic deformation behavior of MPEAs has shown exciting results that coincide with experiments (Smith et al., 2020; Fang et al., 2019; Hua et al., 2021). Understanding the plastic deformation behavior requires knowledge of the dislocation movement through the metal (George et al., 2019). In body-centered cubic (BCC) crystals, dislocation glide can occur on various planes under different conditions and will usually be on the maximum resolved shear stress planes (Mitchell, 1968). The Peierls stress is a measure related to dislocation glide in a pure metal, which is the resolved shear stress required to move a dislocation over at least one lattice site (Zhou et al., 1994). In multicomponent alloy systems, the counterpart of the Peierls stress is the local slip resistance (LSR) (Wang et al., 2020). In a CoCrFeNiMn alloy and its subsystems, the slip resistances calculated by a Peierls-Nabarro model were much larger than those in typical face-centered cubic (FCC) pure metals (Liu et al., 2019). This indicated that the high yield strength of the alloys could be a direct result of the increased slip resistance. Various atomistic simulations have been performed to understand the plastic deformation behavior of both FCC and BCC MPEAs, many of which were discussed by Aitken et al. (2019) and Pei (2018). Recent experimental studies on the plastic deformation behavior of MPEAs highlighted the significance of dislocations. The yield stresses of $Al_{1.2}$CrFeCoNi micropillars were shown to be insensitive to temperature changes, differing from pure metals and dilute alloys (Huang et. al, 2021). The observed temperature insensitivity was attributed to the dynamic recrystallization involving dislocation tangles and formation of dislocation cell structures. Further expansion of the effect of MPEA micropillars used a mixture of molecular dynamics simulations and transmission electron microscopy (TEM) characterization to shed light on deformation mechanisms in these alloys. Both simulations and TEM observations revealed that size effects on yield/flow stress and strain hardening were the result of dislocation mechanisms (Zhang et al., 2021). This indicates that simulations may be a good starting point prior to experiments.

For the dislocation motion to occur, bonds must be broken and formed across the crystalline glide planes, which can be compared to shearing two halves of a crystal across a plane (Hull and Bacon, 2011). The energy required to shear the plane is the generalized stacking fault energy (GSFE) (Vitek, 1992; Vitek, 2011). The GSFE has been used as a baseline measure for designing MPEAs of various chemical compositions (Mayahi, 2020). The addition of small amounts of Co ($0.25 \leq x \leq 2$) to $AlCo_x$CrFeNi was found to enhance the ductility and strength based on the evaluation of GSFE curves, as well as to provide insight into the surface energy values of different slip planes. GSFE calculations are useful for studying the effect of different element concentrations and compositions and how they affect the plastic deformation behavior (Su et al., 2019).

By investigating the plastic deformation behavior of four refractory MPEA alloys using atomistic calculations, one purpose of this study is to evaluate if a high strength, oxidation resistant element containing alloy is possible. Two MPEAs containing Cr, believed to bear good oxidation resistance, CrMoNbTa and CrNbTaW, and two MPEAs known for enhanced strength and ductility (Senkov et al., 2010), MoNbTaV and MoNbTaW, were analyzed. The goal is to further understand the plastic deformation mechanisms that may contribute to these promising properties and evaluate if there are different combinations which have the potential to obtain better properties. To understand the variations in local chemical composition, a common aspect of refractory MPEAs, the GSFE with shear displacement over one lattice periodicity distance was calculated. The GSFE calculations were conducted on three main slip planes in BCC crystals: {110}, {112}, and {123}. The LSR was also calculated for each of the four MPEAs on the same three slip planes. The LSR is the critical resolved shear stress for the glide of a short dislocation by a short distance, employed recently in MoNbTi (Wang et al., 2020; Xu et al., 2021). The mean and standard deviation of GSFE on each plane, and those of LSR for each dislocation type on each plane, are compared across different slip planes and dislocations to understand the effects of variations on local chemical composition and lattice distortion. One motivation for calculating both the GSFE and LSR was to derive the ideal shear strength, which provides another measure of strength, from GSFE, and then compare the two measures of strength to see if there was a correlation. To provide references, the GSFE and Peierls stresses were also calculated in six natural pure metals and four *A*-atom potential-based hypothetical pure metals. Because there exists a dissimilar atomic core structure between edge and screw dislocations in BCC metals and alloys, LSR and Peierls stress calculations were performed for both. Results indicate that the MPEAs containing Cr have higher LSR values and smaller slip resistance anisotropy, which can be attributed to their higher lattice distortion.

2. Materials and methods

LAMMPS (Plimpton, 1995) is used for all molecular statics (MS) simulations in this work. Embedded-atom method (EAM) potentials are used to describe interatomic interactions in four MPEAs: CrMoNbTa, CrNbTaW, MoNbTaV, and MoNbTaW. The six elemental potentials are: Cr (Lin et al., 2008), Mo (Zhou et al., 2004), Nb (Lin et al., 2013), Ta (Zhou et al., 2004), V (Ghafarollahi et al., 2019), W (Zhou et al., 2004). They were validated against density functional theory (DFT) calculations by Xu et al. (2020a) and Xu et al. (2022). Cross interactions between different elements are based on formulations of Johnson (1989) and Zhou et al. (2001). In what follows, this type of interatomic potential is called the ''alloy potential''. All four alloy potentials were used to calculate the basic structural parameters by Xu et al. (2022). Among the four alloy potentials, the one for MoNbTaW has been used by Maresca and Curtin (2020) to study dislocations. Besides the alloy potential, we also used an *A*-atom potential, which provides a mean-field representation of the MPEA by approximating the interactions among different elements as a weighted average (Varvenne et al., 2016). All four *A*-atom potentials have been developed by Xu et al. (2022). While many advanced machine learning-based interatomic potentials are being developed for BCC MPEAs (Byggmästar et al., 2021), they are usually two to three orders of magnitude slower than EAM potentials (Zuo et al., 2020). Thus, they are not practical for a large number of calculations as required in this paper.

To assess the accuracy of all those potentials, we compare the lattice parameter a_0 and three elastic constants C_{11}, C_{12}, and C_{44} for the four MPEAs against those based on DFT. All MS data have been presented by Xu et al. (2022), who also used DFT to calculate the basic structural parameters in the two Cr-containing MPEAs. The structural parameters of one of the two remaining MPEAs, MoNbTaW, have been calculated by DFT (Li et al., 2020a). Thus, we only need to calculate a_0, C_{11}, C_{12}, and C_{44} in MoNbTaV by DFT in this paper. To this purpose, a special quasi-random structure (SQS) (Zunger et al., 1990) was built via ATAT (Van De Walle et al., 2013). Then, following Xu et al. (2022), a_0 was calculated via the relaxation method, while C_{11}, C_{12}, and C_{44} were obtained via the stress-strain method.

Next, we calculate the GSFE curves and LSR in the four MPEAs. For these calculations, SQS were not used. Instead, for each MPEA, a single crystal containing the same type of atoms is built, based on the corresponding lattice parameter of each MPEA. Then, using the "set type/ratio" command in LAMMPS, one quarter of all atoms are randomly replaced with another type of atoms, before another third of remaining atoms are replaced with the third type of atoms, and so on. Eventually, the simulation cell consists of four types of atoms of equal amount. 20 sets of random number seeds are used to produce 20 different atomic structures. Note that even for the same MPEA, simulation cells are separately built for GSFE curves and LSR calculations. The cells for the former are much smaller than those for the latter. The relationship between GSFE and LSR in the same MPEA has been studied by Xu et al. (2021) and will not be investigated here. Our focus in this paper is on comparing the ideal shear stress (derived from GSFE) with LSR across different MPEAs. For the large simulation cells used for LSR calculations, we conduct bond analyses using the cells prior to the insertion of the dislocation and found that the bond length follows a Gaussian distribution in all four MPEAs, as summarized in the Appendix. This finding agrees with those in FCC CoCrCuFeNi (Liu and Wei, 2017) and BCC AlCoCrFeNi MPEAs (Zhang et al., 2021).

Relaxed GSFE curves along the <111> direction on {110}, {112}, and {123} planes were calculated. 41 GSFE values were obtained along each curve, and 20 curves are obtained for each plane type in each MPEA. The cross-sectional areas sampled differed for each MPEA and plane assessed, with the smallest areas on the {112} plane and the largest on the {123} plane. Two key properties of each GSFE curves were calculated, including the unstable stacking fault energy (USFE), γ_{usf}, and the ideal shear strength, T_{is} (Kumar et al., 2020). Readers are referred to Xu et al. (2020a) for more details on simulation cells and calculation method. All input files used in GSFE calculations using alloy potentials for the four MPEAs can be found in this GitHub repository: https://github.com/shuozhixu/FLAM2020-GSFE. To provide references, GSFE curves in Cr and V using elemental potentials and in four MPEAs using *A*-atom potentials are calculated. Note that the GSFE curves in Mo and Nb (Xu et al., 2020a) and Ta and W (Wang et al., 2021) were already calculated in the literature using the same elemental potentials as employed here.

The LSR of edge and screw dislocations on the {110}, {112}, and {123} planes were calculated at 0 K. Based on a random atomic structure, a single dislocation of edge or screw character is inserted by applying the corresponding elastic displacement fields to all

Table 1
Lattice parameter and elastic constants for pure metals including both MS and experimental values.

	Method	a_0 (Å)	C_{11} (GPa)	C_{12} (GPa)	C_{44} (GPa)	A_c
Cr	MS (Xu et al., 2022)	2.881	398.03	93.45	103.56	0.68
	Exp (Warlimont and Martienssen, 2018)	2.885	348	67	100	0.71
Mo	MS (Xu et al., 2020a)	3.135	458.76	167.84	114.32	0.79
	Exp (Warlimont and Martienssen, 2018)	3.147	465	163	109	0.72
Nb	MS (Xu et al., 2020a)	3.3	263.56	125.28	35.03	0.51
	Exp (Warlimont and Martienssen, 2018)	3.301	245	132	28.4	0.5
Ta	MS (Xu et al., 2022)	3.303	262.59	157.74	82.33	1.57
	Exp (Warlimont and Martienssen, 2018)	3.303	264	158	82.6	1.56
V	MS (Xu et al., 2022)	3.026	263.93	120.19	38.37	0.53
	Exp (Warlimont and Martienssen, 2018)	3.024	230	120	43.1	0.78
W	MS (Xu et al., 2022)	3.165	522.54	204.22	160.76	1.01
	Exp (Warlimont and Martienssen, 2018)	3.165	523	203	160	1

Table 2
Lattice parameter and elastic constants of MPEAs calculated through MS and DFT and experimental values (when available). Spin-polarization is not considered in any DFT calculations. Subscripts *A* and V denote results from *A*-atom potentials and simple rule of mixtures, respectively.

	Method	a_0 (Å)	C_{11} (GPa)	C_{12} (GPa)	C_{44} (GPa)	A_c
CrMoNbTa	MS (Xu et al., 2022)	3.171	320.33	144.34	68.68	0.78
	MS_A (Xu et al., 2022)	3.175	262.11	111.36	54.28	0.72
	MS_V (Xu et al., 2022)	3.16	330.50	130.00	80.00	0.80
	DFT (Xu et al., 2022)	3.179	333.89	145.19	58.69	0.62
CrNbTaW	MS (Xu et al., 2022)	3.179	333.18	161.81	82.03	0.96
	MS_A (Xu et al., 2022)	3.188	277.43	127.31	64.21	0.86
	MS_V (Xu et al., 2022)	3.16	345.00	140.00	92.75	0.90
	DFT (Xu et al., 2022)	3.189	332.1	161.93	60.2	0.71
MoNbTaV	MS (Xu et al., 2022)	3.206	263.72	144.15	66.43	1.11
	MS_A (Xu et al., 2022)	3.204	263.32	144.69	68.91	1.16
	MS_V (Xu et al., 2022)	3.19	301.00	143.25	65.78	0.83
	DFT	3.211	282.56	153.47	33.07	0.51
	Exp (Yao et al., 2016b)	3.208	-	-	-	-
MoNbTaW	MS (Xu et al., 2022)	3.221	351.55	172.27	92.18	1.03
	MS_A (Xu et al., 2022)	3.221	351.91	174.13	95.79	1.08
	MS_V (Xu et al., 2022)	3.23	374.25	164.00	95.00	0.90
	DFT (Li et al., 2020a)	3.242	377	160	69	0.64
	Exp (Senkov et al., 2010)	3.2134	-	-	-	-

atoms. By assigning appropriate boundary conditions, we had periodic array of dislocations models. Then a shear strain that was incrementally (10^{-6} per step for screw and 10^{-5} per step for edge) increased was applied to each model until the dislocation moved by at least 1 nm. For each dislocation on each plane in each MPEA, a set of 20 LSR values was obtained. For each set, the mean, standard deviation, and coefficient of variation (COV), the last of which is the ratio of the standard deviation to the mean value, are then determined. Readers are referred to Xu et al. (2021) for more details on simulation cells and calculation method. All input files used in LSR calculations for the four MPEAs using alloy potentials can be found in this GitHub repository: https://github.com/shuozhixu/FLAM2020-LSR. To provide references, Peierls stresses in four pure BCC metals (Cr, Ta, V, and W) using elemental potentials and in four MPEAs using *A*-atom potentials are calculated. Note that the Peierls stresses in Mo and Nb were already calculated by Xu et al. (2021). All input files used in Peierls stress calculations can be found in this GitHub repository: https://github.com/shuozhixu/FLAM2020-PS.

We note that the effects of chemical ordering on dislocations in some BCC MPEAs (including MoNbTaW) have been studied via atomistic simulations in the literature (Antillon et al., 2021; Zhao et al., 2021; Yin et al., 2021; Mishra et al., 2021). Therefore, we are not studying them in this paper.

3. Results

3.1. Lattice parameter and elastic constants

Table 1 provides the lattice parameters, a_0, elastic constants C_{11}, C_{12}, and C_{44}, and the Zener ratios, calculated by MS for the six pure metals. Table 2 provides the same quantities for the four MPEAs based on the alloy potentials, as well as those based on the *A*-atom potentials and simple rule of mixtures. As mentioned, the basic structural parameters in CrMoNbTa and CrNbTaW based on MS were already compared against DFT by Xu et al. (2022). For MoNbTaV and MoNbTaW MPEAs, the calculated lattice parameters are consistent with the available experimental values for the alloys. In all MPEAs, the values calculated using the *A*-atom potentials and simple rule of mixtures are in good agreement with the alloy potential, DFT, and experimental values (when available). In the two Cr-containing MPEAs, the *A*-atom potential-based elastic constants are lower than those based on the alloy potentials. In MoNbTaW

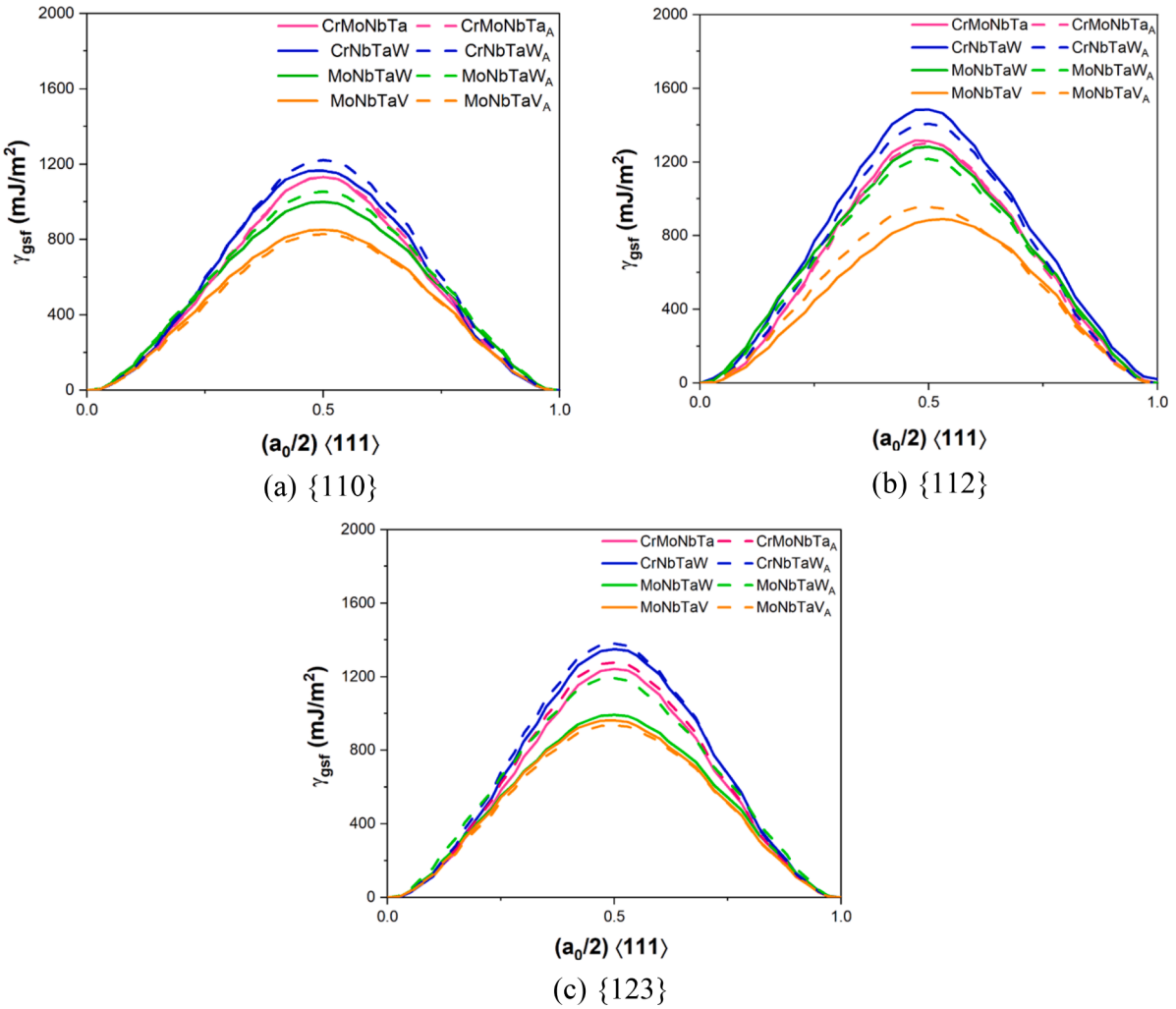

Fig. 1. GSFE curves of four MPEAs on (a) {110}, (b) {112}, and (c) {123} planes based on MS simulations using the alloy and *A*-atom potentials (subscript "A").

and MoNbTaV, elastic constants using the *A*-atom and alloy potentials are similar. The differences in basic structural parameters between *A*-atom and alloy potentials were recently found to scale positively with the lattice distortion (Xu et al., 2022).

The Zener ratio, A_c, is applied as a measure of the cubic elastic anisotropy, in which a value of unity represents ideal isotropy. Three of the MPEAs are nearly isotropic ($A_c^{MoNbTaW}$= 1.03, $A_c^{MoNbTaV}$= 1.11, $A_c^{CrNbTaW}$= 0.96) and one is elastically anisotropic ($A_c^{CrMoNbTa}$= 0.78) according to the alloy potentials. Results based on the simple rule of mixtures are similar but are slightly deflated in MoNbTaV and MoNbTaW. DFT calculations predict lower values of A_c, and all four MPEAs are considered anisotropic.

3.2. *Generalized stacking fault energy*

The GSFE curves on all three slip planes in four MPEAs are presented in Fig. 1. The calculations span displacements over one periodicity distance along the *z* <111> direction, which is the Burgers vector magnitude of a full dislocation, *b*. The GSFE curves based on both alloy and *A*-atom potentials are shown.

The GSFE curves all reach a single peak value within the periodic length *b*. This peak value is generally termed the USFE, γ_{usf}, and therefore there are no local minimum or metastable states. Pure BCC metals exhibit GSFE curves with this particular characteristic as well (Xu et al., 2020a, 2020b; Wang et al., 2021).

The GSFE curves based on the alloy potentials exhibit a slight deviation from those based on the *A*-atom potentials, indicating an MPE effect that is the variation caused by the natural mixture of elements. As a result, even on the {110} plane, for which the pure metals' GSFE curves are symmetric, the USFE does not occur at a half lattice shift (*b*/2) in most MPEAs. This suggests that a single GSFE calculation at *b*/2 may not provide an accurate USFE. This is related to the variation in local atomic arrangement in which the MPEA curve is sampled and suggests anisotropy in resistance to dislocation glide (Xu et al., 2020a).

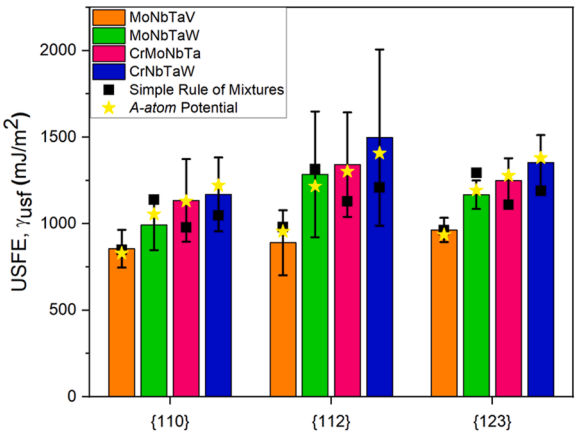

USFE Coefficient of Variation			
	{110}	{112}	{123}
CrMoNbTa	0.2108	0.2249	0.1045
CrNbTaW	0.1823	0.3398	0.1174
MoNbTaV	0.1269	0.2113	0.0724
MoNbTaW	0.1462	0.2831	0.0704

Fig. 2. Mean USFE values of four MPEAs in three slip planes. For the alloy potentials, standard deviation and COV are also presented.

Table 3
USFE values (in mJ/m^2) of pure metals from both MS and DFT calculations. For Cr, DFT results without spin-polarization are presented.

	Method	{110}	{112}	{123}
Cr	MS	1096	1265	1243
	DFT (Xu et al., 2020b)	1565	1608	1628
Mo	MS (Xu et al., 2020a)	1458	1689	1658
	DFT (Xu et al., 2020b)	1443	1465	1481
Nb	MS (Xu et al., 2020a)	605	697	685
	DFT (Xu et al., 2020b)	677	769	767
Ta	MS (Wang et al., 2021)	751	868	852
	DFT (Xu et al., 2020b)	724	838	832
V	MS	581	669	657
	DFT (Xu et al., 2020b)	701	816	792
W	MS (Wang et al., 2021)	1740	2011	1976
	DFT (Xu et al., 2020b)	1773	1846	1854

Results of the mean USFE values are summarized in Fig. 2. On all three planes, CrNbTaW obtains the highest average USFE value, with the highest being in the {112} plane. Specifically, the following order

$$\gamma_{usf}^{MoNbTaV} < \gamma_{usf}^{MoNbTaW} < \gamma_{usf}^{CrMoNbTa} < \gamma_{usf}^{CrNbTaW}$$

holds on all three planes. For reference, the USFE values of the pure metals are listed in Table 3. The USFE values of the pure metals on all three slip planes follow the order

$$\gamma_{usf}^{V} < \gamma_{usf}^{Nb} < \gamma_{usf}^{Ta} < \gamma_{usf}^{Cr} < \gamma_{usf}^{Mo} < \gamma_{usf}^{W}$$

It is shown that γ_{usf}^{W} is approximately 300 mJ/m^2 higher than γ_{usf}^{Mo} on all three slip planes considered. As a result, the presence of W in CrNbTaW, as opposed to Mo in CrMoNbTa, can possibly explain the former's higher γ_{usf}. The same explanation can be applied to the difference between the MoNbTaW and MoNbTaV MPEAs and that between the CrMoNbTa and MoNbTaV MPEAs. Since γ_{usf}^{V} is the lowest among all pure metals, it is expected to contribute to a lower overall value in the MPEAs. Of the three planes studied for all pure metals and the four MPEAs, the {112} plane consistently attains the highest USFE value. Taken together, the highest USFE value was obtained by CrNbTaW on the {112} plane.

It may be expected that the combination of Mo and W would always yield an MPEA with the highest γ_{usf} value; however, this is not the case. As shown in Fig. 2, the simple rule of mixtures estimation for $\gamma_{usf}^{MoNbTaW}$ on the {110} plane is 1139 mJ/m^2, while the estimation of $\gamma_{usf}^{CrMoNbTa}$ and $\gamma_{usf}^{CrNbTaW}$ are 978 and 1048 mJ/m^2, respectively. However, based on the alloy potentials, the mean $\gamma_{usf}^{CrMoNbTa}$ and $\gamma_{usf}^{CrNbTaW}$ values on the {110} plane are respectively 76 and 166 mJ/m^2 higher than the mean $\gamma_{usf}^{MoNbTaW}$. These indicate that γ_{usf} cannot solely be considered on the basis of constituent elements and their proportions, and so an estimation of γ_{usf} using a simple rule of mixtures may not be accurate. Results based on the *A*-atom potentials are also included in Fig. 2. They are in close agreement with those based on alloy potentials, indicating that calculations using *A*-atom potentials may provide more accurate estimates of γ_{usf} than the simple rule of mixtures.

The variation among curves of the same plane type in the same MPEA is due to the variation in local chemical composition. Depending on the random atomic arrangement that was surveyed, peak values may have occurred at large ranges of values causing a large COV in USFE. The COV for each plane in each MPEA is presented in Fig. 2. The variation is related to the size of the sampled area (Zhao et al., 2019a). The smallest cross-sectional area used was in the {112} plane, approximately 12 Å^2, while the {123} plane had the

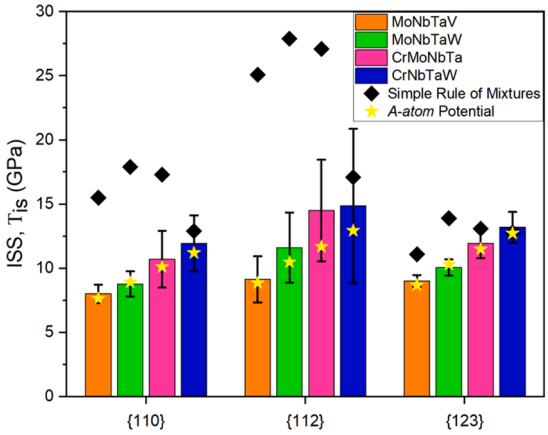

ISS Coefficient of Variation			
	{110}	{112}	{123}
CrMoNbTa	0.2066	0.2727	0.0971
CrNbTaW	0.1817	0.4041	0.0903
MoNbTaV	0.0883	0.1979	0.0514
MoNbTaW	0.1116	0.2347	0.0627

Fig. 3. Mean ideal shear strength (ISS) values of four MPEAs in three slip planes. For the alloy potentials, standard deviation and COV are also presented.

Table 4
Ideal shear strength values (in GPa) of the reference pure metals based on both MS and DFT calculations. For Cr, DFT results without spin-polarization are presented.

	Method	{110}	{112}	{123}
Cr	MS	13.3	15.3	15.1
	DFT (Xu et al., 2020b)	20.8	26.1	24.65
Mo	MS (Xu et al., 2020a)	33.1	58.4	19.3
	DFT (Xu et al., 2020b)	17.7	21.7	20.4
Nb	MS (Xu et al., 2020a)	14.1	24.5	8.1
	DFT (Xu et al., 2020b)	7.5	9.9	8.9
Ta	MS (Wang et al., 2021)	8.7	10.1	9.9
	DFT (Xu et al., 2020b)	7.8	11.4	10
V	MS	6.2	7.2	7.1
	DFT (Xu et al., 2020b)	8.3	10.8	9.7
W	MS (Wang et al., 2021)	15.6	18.4	18.1
	DFT (Xu et al., 2020b)	21	26.5	25

largest cross-sectional area, approximately 58 Å^2. The increase in the cross-sectional area leads to a lower COV, hence the lowest COV value on the {123} plane and the highest COV on the {112} plane. The Cr-containing MPEAs have not only higher overall USFE values, but also higher standard deviations and higher COV. The COV exhibits the MPE effect, which may be also related to the presence of Cr that causes increased lattice distortion.

The ideal shear strength (T_{is}) is calculated as the maximum value of the gradient of the GSFE curve. Fig. 3 shows the mean values of T_{is}, as well as the standard deviation and COV. For reference, the T_{is} values in the six pure metals are presented in Table 4. Like the USFE, CrNbTaW achieves the highest value on all three planes, with the highest value on the {112} plane. The order also follows the same as seen in the USFE,

$$T_{is}^{MoNbTaV} < T_{is}^{MoNbTaW} < T_{is}^{CrMoNbTa} < T_{is}^{CrNbTaW}$$

A larger standard deviation is associated with a higher T_{is} value. The large variation is once again related to a difference in local chemical composition and atomic arrangement due to the different crystallographic planes that may be sampled. For comparison, the values for the *A*-atom potential and estimation using simple rule of mixtures are included. Similar to the USFE, results based on the *A*-atom potentials are close to those based on the alloy potentials, indicating that the former provide a relatively accurate representation of T_{is}. Unlike the *A*-atom potential, the simple rule of mixtures largely overestimates T_{is}. The largest difference was seen in the {110} and {112} planes in the three MPEAs containing Mo. This difference is most likely due to the high T_{is} values obtained in both planes for Mo, which inflate the simple rule of mixtures calculation. This indicates that the values for pure metals used to calculate T_{is} must be accurate or the simple rule of mixtures will not be a reliable model. Note that the simple rule of mixtures-based T_{is} for the MPEA that does not contain Mo, i.e., CrNbTaW, are also overestimated, albeit by a lesser amount, on the {110} and {112} planes.

3.3. Local slip resistance

3.3.1. Peierls stresses in pure metals and A-atom potential-based MPEAs

The Peierls stresses of both screw and edge dislocations in pure metals and MPEAs using the *A*-atom potentials on three planes — {110}, {112}, and {123} — are presented in Table 5. Values for the Peierls stress were all calculable for edge dislocations; however,

Table 5
Peierls stresses or LSR, in units of MPa, of (a) pure metals, (b) MPEAs based on simple rule of mixtures estimation, (c) MPEAs based on *A*-atom potentials, and (d) MPEAs based on alloy potentials.

(a) Peierls stresses in six pure meatls

Plane	Dislocation	Cr	Mo (Xu et al., 2021)	Nb (Xu et al., 2021)	Ta	V	W
{110}	Edge	102	50	6	13	9	55
	Screw	3631	-	-	-	-	-
{112}	Edge	900	533	118	276	119	411
	Screw	-	2496	859	2137	817	3427
{123}	Edge	245	160	12	30	10	86
	Screw	-	-	-	-	-	-

(b) Simple rule of mixtures estimation of the LSR in MPEAs using the reference pure metals Peierls stresses

Plane	Dislocation	$CrMoNbTa_V$	$CrNbTaW_V$	$MoNbTaW_V$	$MoNbTaV_V$
{110}	Edge	43	44	31	20
	Screw	-	-	-	-
{112}	Edge	457	426	335	262
	Screw	-	-	2230	1577
{123}	Edge	112	93	72	53
	Screw	-	-	-	-

(c) Peierls stresses in four MPEAs using the *A*-atom potentials

Plane{110}	Dislocation	$CrMoNbTa_A$	$CrNbTaW_A$	$MoNbTaW_A$	$MoNbTaV_A$
	Edge	4.45	4.74	4.09	4.18
	Screw	-	-	-	-
{112}	Edge	41.9	5.65	84.15	9.005
	Screw	795.9	810.3	1158.4	335.76
{123}	Edge	3.168	3.47	5.25	2.95
	Screw	-	-	-	-

(d) Mean LSR values in four MPEAs using the alloy potentials. Note, there is no standard deviation for the MoNbTaW screw dislocation on the {110} plane as there was only one calculable result.

Plane	Dislocation	CrMoNbTa		CrNbTaW		MoNbTaW		MoNbTaV	
		Mean	Std. Dev.	Mean	Std. Dev.	Mean	Std. Dev.	Mean	Std. Dev.
{110}	Edge	2003	1046	2183	937	912	402	1011	465
	Screw	2009	718	2619	405	1391	-	1274	202
{112}	Edge	1916	710	2115	882	1566	468	1188	364
	Screw	2405	620	2007	777	1421	553	1281	541
{123}	Edge	2011	525	2079	764	912	409	676	335
	Screw	2050	829	1822	856	1789	584	1130	269

many cases were *incalculable* for screw dislocations. An incalculable Peierls stress or incalculable LSR refers to when the screw dislocation is unstable and cross-slips and hence the critical stress for the habit plane cannot be calculated. Discussions of incalculable screw dislocation Peierls stresses and LSR have been presented by Xu et al. (2021). Among all screw dislocations, on the {110} plane only the Peierls stress in Cr was calculable, while the Peierls stresses in all pure metals but Cr were calculable on the {112} plane. There were no calculable screw Peierls stresses on the {123} plane for any pure metals. On all three planes, Cr has the highest Peierls stress among the six pure metals considered. With the *A*-atom potentials, none of the screw dislocation Peierls stresses in the {110} or {123} planes was calculable, while all were calculable in the {112} plane. All edge dislocations on all planes were once again calculable. The calculated values on the {110} plane for the edge dislocations were all similar, ranging from 4.09 MPa for $MoNbTaW_A$ to 4.74 MPa for $CrNbTaW_A$. However, this is not the case for either {112} or {123} plane, on which $MoNbTaW_A$ obtains the highest Peierls stress for edge dislocations.

3.3.2. LSR values: mean and distribution

The mean and standard deviation of the 20 calculated LSR values for the MPEAs are presented in Table 5, where estimations of LSR in the MPEAs following the simple rule of mixtures are also included. Among all mean LSR, CrNbTaW had the highest value of 2619 MPa on the {110} plane for the screw dislocation. This could not be compared to the Peierls stress of $CrNbTaW_A$ or the simple rule of mixtures-based value, as both were incalculable. In all cases, the mean LSR value was higher for the same MPEA than the corresponding Peierls stress using the *A*-atom potential. For both edge and screw dislocations on all planes, the Cr-containing MPEAs had a higher mean LSR value than those without Cr. A higher mean LSR in the MPEAs containing Cr can be attributed to two factors: (1) a higher lattice distortion and (2) Cr among all six pure metals has the highest Peierls stress. The effect of the lattice distortion will be discussed in Section 3.4.

On the three identified planes, the Peierls stress in Cr is nearly double the amount of the next closest value (either Mo or W) in edge dislocations. In all the edge dislocation calculations, the LSR values obtained following simple rule of mixtures were much lower than those based on the alloy potentials but seem better than the results obtained from the *A*-atom potentials. This comparison indicates that estimating the LSR of MPEAs via the simple rule of mixtures or *A*-atom potentials is not an accurate representation of the minimum resolved shear stress required to move a short dislocation.

Fig. 4 shows the distribution of LSR values on all planes, {110}, {112}, and {123}, for both edge and screw dislocations. On the {110} plane for edge dislocations, the Cr-containing MPEAs have a large variation across the distribution. CrMoNbTa has a range of

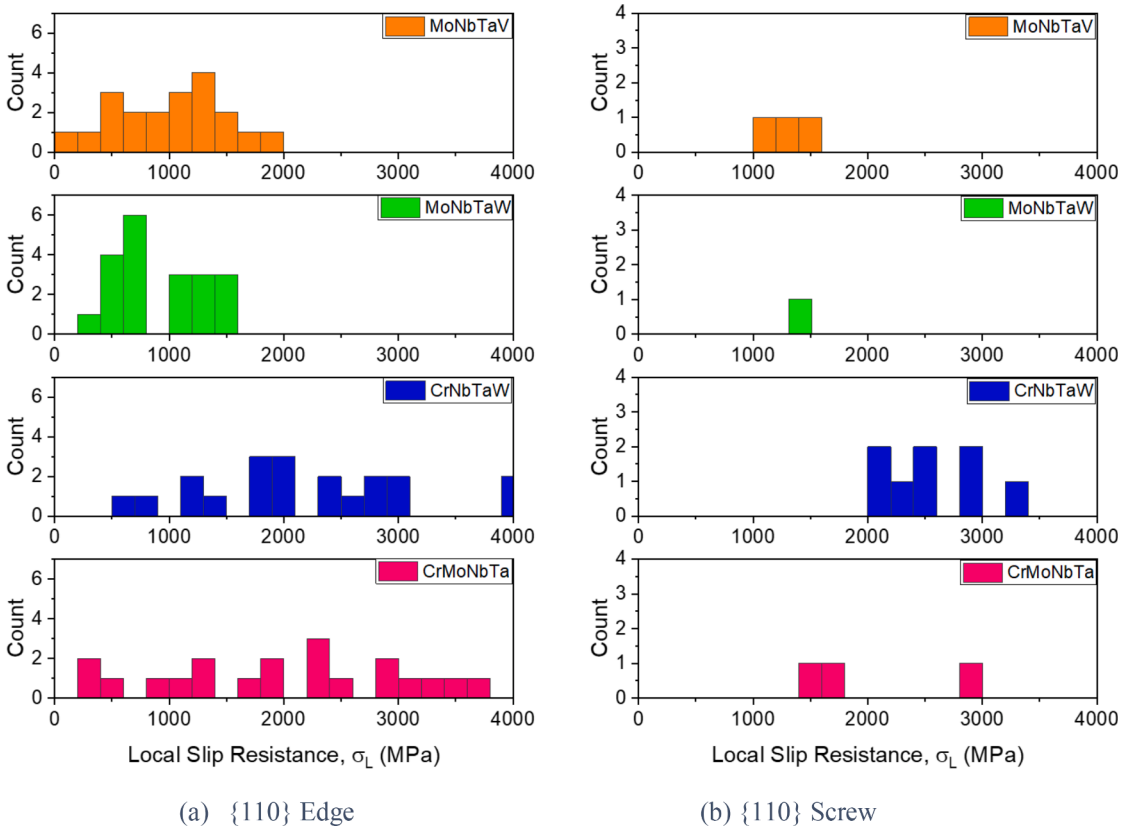

Fig. 4. Distribution of the LSR in the four MPEAs for (a) edge dislocations on the {110} plane, (b) screw dislocations on the {110} plane, (c) edge dislocations on the {112} plane, (d) screw dislocations on the {112} plane, (e) edge dislocations on the {123} plane, and (f) screw dislocations on the {123} plane.

3444 MPa and CrNbTaW has a range of 3366 MPa, while MoNbTaW and MoNbTaV have ranges of 1353 MPa and 1651 MPa, respectively. Unlike the edge dislocation, the LSR of many screw dislocations were incalculable. CrNbTaW had the most calculable results among the four MPEAs with 8 out of 20 results. The MoNbTaW MPEA had the least number of calculable results with only 1 out of 20, while both CrMoNbTa and MoNbTaV had 3 out of 20.

Like the {110} plane for edge dislocations, the Cr-containing MPEAs have a larger distribution for the edge dislocations, ranging from 398 to 3286 MPa for CrMoNbTa and 332 to 3302 MPa for CrNbTaW in the {112} plane. Despite a large variation, the mean LSR values of the Cr-containing MPEAs are higher. CrMoNbTa has 10 out of the 20 results and CrNbTaW has 11 out of 20 results above 2000 MPa. MoNbTaW has only 5 out of the 20 LSR values above 2000 MPa, while MoNbTaV has none. For the same MPEA, the screw dislocations in the {112} plane had a larger number of calculable LSR than those in the {110} plane. Once again, the Cr-containing MPEAs have a larger standard deviation and also higher values of mean LSR compared to those without Cr.

On the {123} plane, the mean and distribution of LSR are similar to those in the {110} and {112} planes. CrMoNbTa and CrNbTaW vary over a large range but have more counts above 2000 MPa. MoNbTaW has only one count above 2000 MPa while MoNbTaV does not have any. For the screw dislocations in the {123} plane, the results were calculable for approximately half of the time among all MPEAs.

3.3.3. Slip resistance anisotropy

Understanding the plastic anisotropy in BCC metals has proved significant since its mechanism is not as well understood as it is in FCC metals . Xu et al. (2021) proposed two measures of slip resistance anisotropy in MoNbTi. Wang et al. (2021) then applied them to four BCC pure metals. One measure is based on the Peierls stress or LSR among different slip planes. When considering the ranking of the Peierls stress in pure metals, all six elements follow the order $\sigma_p^{\{110\}} < \sigma_p^{\{123\}} < \sigma_p^{\{112\}}$. Dislocation glide has been considered and experimentally studied most frequently on the {110} plane, described as an elementary slip plane (Srivastava et al., 2013; Lim et al., 2013). The findings in pure metals match previous studies that dislocation glide occurs the easiest on the {110} plane. When

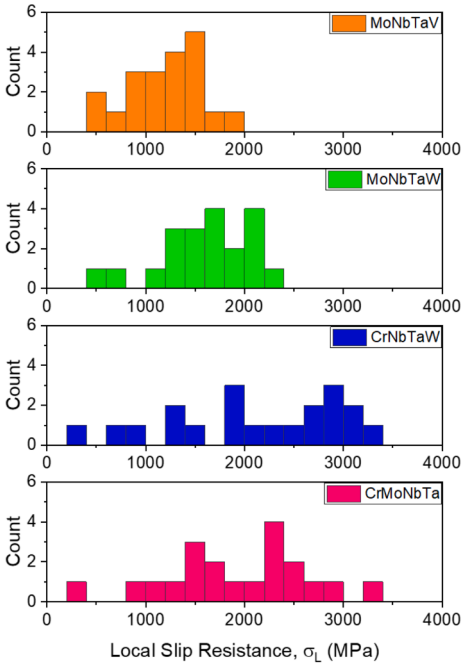

(c) {112} Edge

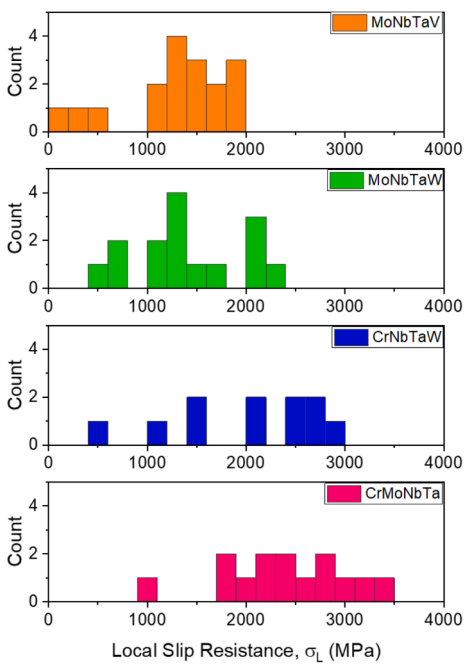

(d) {112} Screw

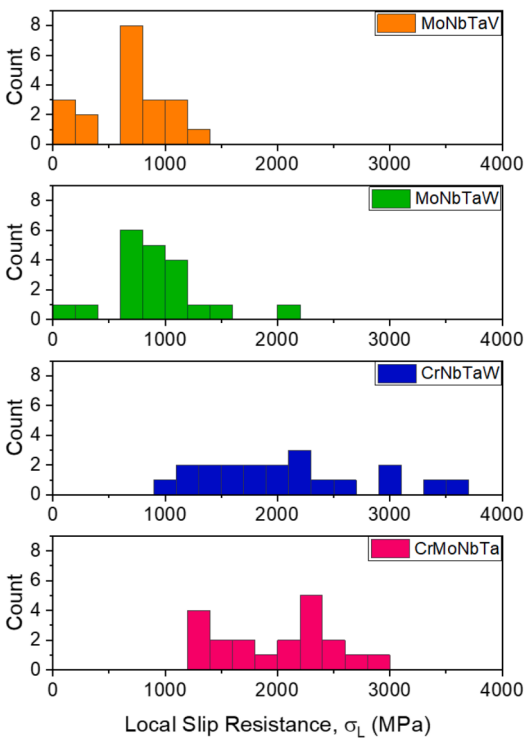

(e) {123} Edge

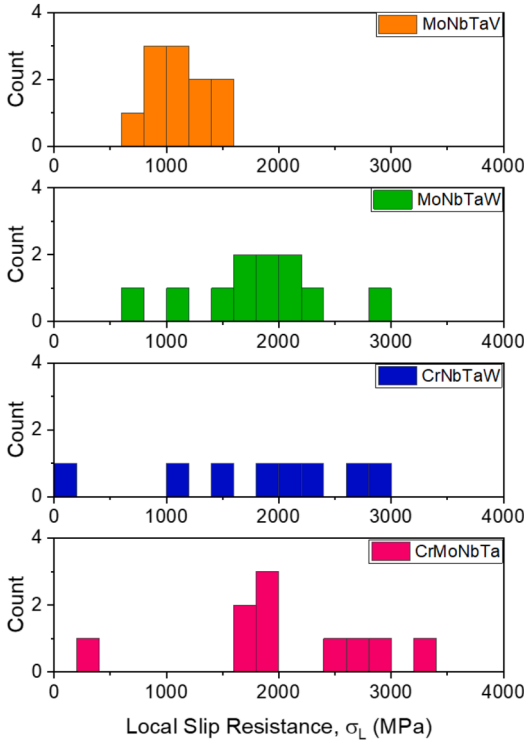

(f) {123} Screw

Fig. 4. (*continued*).

Table 6
Slip resistance anisotropy in MPEAs and pure metals for edge or screw dislocations.

(a) Four MPEAs based on alloy potentials across all three planes for each dislocation type.						
	CrMoNbTa	CrNbTaW	MoNbTaV	MoNbTaW		
Edge	0.027	0.025	0.279	0.346		
Screw	0.101	0.196	0.069	0.145		
(b) Four MPEAs based on *A*-atom potentials across all planes for the edge dislocation.						
	$CrMoNbTa_A$	$CrNbTaW_A$	$MoNbTaV_A$	$MoNbTaW_A$		
Edge	2.622	0.242	0.666	3.768		
(c) Six pure metals across all planes for the edge dislocation.						
	Cr	Mo	Nb	Ta	V	W
Edge	1.507	1.561	3.088	3.094	2.868	1.580

Table 7
Screw-to-edge ratios in Peierls stresses or LSR in (a) pure metals, (b) MPEAs with *A*-atom potentials, and (c) MPEAs with alloy potentials.

(a) Peierls stresses in pure metals						
Plane	Cr	Mo	Nb	Ta	V	W
{110}	35.6	-	-	-	-	-
{112}	-	4.68	7.28	7.74	6.87	8.34
{123}	-	-	-	-	-	-
(b) Peierls stresses in *A*-atom potential-based MPEAs.						
Plane	$CrMoNbTa_A$	$CrNbTaW_A$	$MoNbTaW_A$	$MoNbTaV_A$		
{110}	-	-	-	-		
{112}	19.0	143.4	13.8	37.3		
{123}	-	-	-	-		
(c) LSR in alloy potential-based MPEAs.						
Plane	CrMoNbTa	CrNbTaW	MoNbTaW	MoNbTaV		
{110}	1.003	1.200	1.526	1.260		
{112}	1.255	0.949	0.908	1.078		
{123}	1.019	0.876	1.961	1.671		

considering the mean LSR values of edge dislocations of the MPEAs, this ranking no longer matches. The results indicate that glide occurs the easiest on the {112} plane and hardest on the {123} plane in CrMoNbTa. In contrast, glide is the easiest on the {123} plane and most difficult on the {110} plane in CrNbTaW. Such findings differ from the pure metal behavior. Though the rankings differ, the ranges of the mean values among different planes are very small, 95 MPa and 104 MPa, respectively in the two alloys for the edge dislocations. This suggests that slips may occur on any of the three planes and could depend on the local chemical environment. MoNbTaW matches the pure metal behavior in that the slip is easiest on the {110} plane and most difficult on the {112} plane based on the mean LSR values. Similarly, glide is the hardest on the {112} plane in MoNbTaV, while it is the easiest on the {123} plane. In MoNbTaW, the glide is equally probable on the {110} and {123} planes, since both mean LSR for the edge dislocation are 912 MPa; however, the difference in mean values between the {110} and {123} planes of MoNbTaV is much larger: 512 MPa. The ranges of mean values of MoNbTaW and MoNbTaV are 654 and 512 MPa respectively. This shows that slip is significantly more difficult on the {112} plane for these two MPEAs. To quantify the slip resistance anisotropy among different slip planes, we calculated the COV in Peierls stresses and LSR among the three planes for edge and screw dislocations, respectively. Results are summarized in Table 6. It is shown that the slip resistance anisotropy is the highest for edge dislocations in MoNbTaW with a value of 0.346, and the anisotropy in MoNbTaV is similar at 0.279. The two Cr-containing MPEAs have much lower anisotropy for edge dislocations at 0.027 and 0.025 respectively. This behavior does not follow suit for the screw dislocations, as CrNbTaW has the highest slip resistance anisotropy of 0.196 while MoNbTaV possesses the lowest value at 0.069. Overall, in the MPEAs, the two Cr-containing ones, which have larger lattice distortion, have smaller slip resistance anisotropy than the other two MPEAs. The MPEAs' anisotropy is much smaller than those in *A*-atom potential-based MPEAs and pure metals, which are also presented in Table 6.

Another measure of the slip resistance anisotropy is the screw-to-edge ratio on the same slip plane. Table 7 reports these ratios in pure metals, *A*-atom potential-based MPEAs, and alloy potential-based MPEAs. Since the Peierls stresses or LSR of some screw dislocations were incalculable, not all ratios could be determined. Our results indicate a significantly decreased ratio in the MPEAs than in the pure metals. On the {110} plane, only Cr can be compared, as the rest of the screw dislocations of the pure metals were unstable. The ratios of the MPEAs are much lower at 1.003 and 1.2 respectively for CrMoNbTa and CrNbTaW, compared to the much larger value of 35.6 for Cr. On the {112} plane, the ratio for every pure metal except Cr could be determined. The ratios of the MPEAs range from 0.908 to 1.255 which are approximately four to eight times less than the values for pure metals. None of the pure metals could be compared on the {123} plane, as none of the screw dislocations Peierls stresses were calculable. The *A*-atom potential-based ratios could only be determined on the {112} plane and, when compared to the alloy potential-based MPEAs, they are much higher.

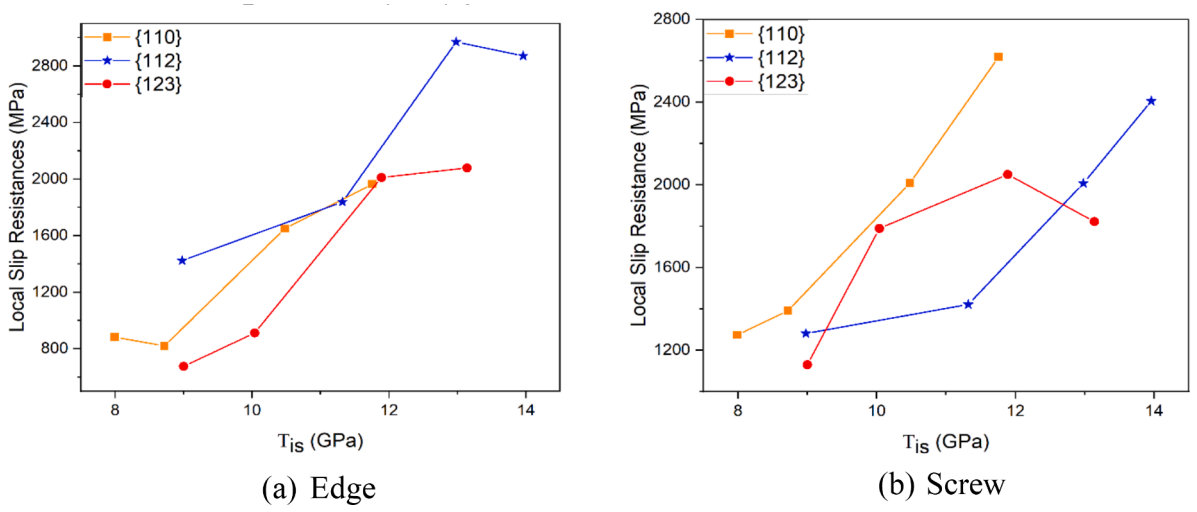

Fig. 5. Mean local slip resistance (in MPa) versus the ideal shear strength (in GPa) for (a) edge and (b) screw dislocations in four MPEAs.

Table 8
Lattice distortion δ values of the four MPEAs.

	CrMoNbTa	CrNbTaW	MoNbTaV	MoNbTaW
δ	0.0545	0.0543	0.0367	0.0237

CrMoNbTa has the lowest ratio on the {110} plane, however, all are relatively similar, with a range of only 0.252. CrNbTaW differs, in that the {123} plane contains the lowest ratio, however, the range is still not large, only 0.324. Both MoNbTaV and MoNbTaW have the lowest ratios on the {112} plane, being 0.908 and 1.079 respectively. While these have low values, they do have a larger range on the three planes of 0.593 and 1.053. Low screw-to-edge ratios in LSR have previously been reported (Xu et al., 2021), but only in one MPEA: MoNbTi. Here, our results show that the screw-to-edge ratios in LSR are generally lower in MPEAs with higher lattice distortion. In MoNbTaW, which has the lowest lattice distortion among the four MPEAs, previous atomistic simulations found that the edge-to-screw ratio in mobility on the {110} plane is as high as 20 at 300 K (Yin et al., 2021) and the dislocation loop expansion left no debris behind, unlike other BCC MPEAs with larger lattice distortion (Chen et al., 2020).

3.3.5. Correlation between the ideal shear strength and the mean LSR

As previously mentioned, the motivation for calculating both the GSFE curves and the LSR values was to compare the ideal shear strength, obtained from the GSFE curve, with the LSR. Fig. 5 presents the ideal shear strength on each plane versus the mean LSR value for both edge and screw dislocations. The correlation between the ideal shear strength and the LSR is generally positive. The {112} plane generally obtains a higher ideal shear strength and LSR for edge dislocations. The {110} and {123} planes obtained similar values with respect to each other. For the screw dislocations, the {110} plane had the strongest positive correlation, followed by the {112} plane.

3.4. Lattice distortion

The effect of local lattice distortion induced by the atomic size mismatch is one of the four core effects of MPEAs that contribute to their superior mechanical properties (Yeh, 2015). The energy caused by the lattice distortion in combination with the high configurational entropy of mixing may significantly contribute to the thermodynamic stability of these alloys. In any alloy potential-based MPEAs, lattice distortion was naturally introduced following energy minimization. To quantify the lattice distortion, we calculated the atomic size mismatch by

$$\delta = 100\sqrt{\sum_{i=1}^{n} c_i\left(1-\frac{r_i}{\bar{r}}\right)} \tag{1}$$

where $\bar{r} = \sum_{i=1}^{n} c_i r_i$ with c_i and r_i being the atomic percentage and atomic radius of element i, respectively (Song et al., 2017). Here, the

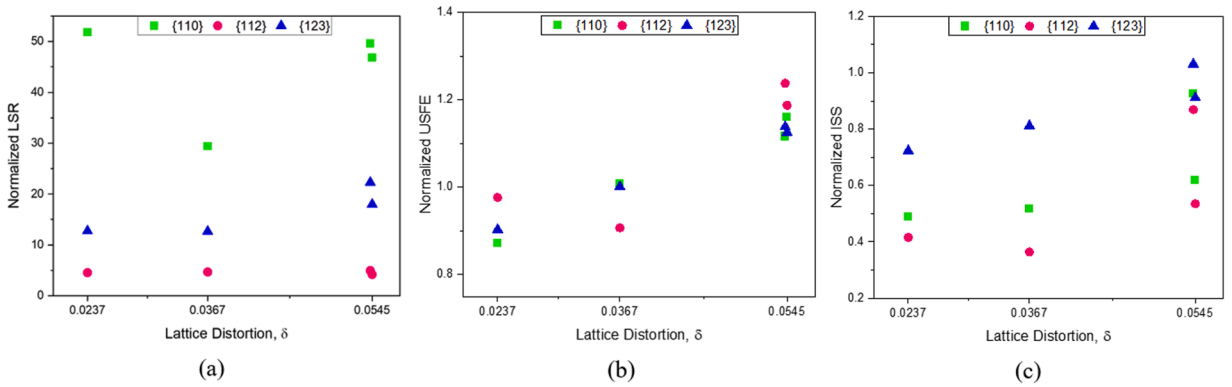

Fig. 6. Plot of (a) normalized LSR, (b) normalized USFE, and (c) normalized ideal shear strength, with respect to the lattice distortion, in four MPEAs.

atomic percentage for each component is 25% and the atomic radii can be derived from the lattice parameters of the six pure metals (Table 1). Note that there is no lattice distortion in any pure metals or in any *A*-atom potential-based MPEAs. Table 8 shows the lattice distortion in the four MPEAs calculated from Eq. (1). Of the six elements used, Cr has the smallest atomic radius and is considerably lower than those of Nb and Ta. Thus, the Cr-containing MPEAs had a higher mismatch estimation than those without Cr, as found by Xu et al., (2022). In MPEAs, the lattice disortion is believed to be a significant contribution to their strengths (Lee et al., 2020; Oh et al., 2021; Li et al., 2020b; Roy et al., 2021; Kim et al., 2021a; Kim et al., 2021b; Zhao et al., 2019b; Zhao and Nieh, 2017). Lattice distortion has also been shown to be influential on the dislocation behavior in MPEAs (Li et al., 2020c), where local stress fields are created, causing a dislocation line to bend and thus enhancing glide resistance.

When comparing two MPEAs, there are usually two differences: chemical compositions and lattice distortion. Both factors might contribute to the mechanical properties such as strength. To understand which of the factors may play a more significant role, the quotient of the LSR by the simple rule of mixtures estimation was calculated, noted as the normalized LSR, which was plotted with respect to the lattice distortion in Fig. 6(a). Similar plots are presented for the normalized USFE and normalized ideal shear strength, respectively, in Fig. 6(b) and Fig. 6(c). Since not all values of the simple rule of mixtures were calculable for the screw dislocations, only the edge dislocations were considered here. On the {110} plane, the normalized LSR in MoNbTaW is higher than both Cr-containing MPEAs. This result shows that lattice distortion effects are not the primary factor for strengthening on this plane. On the {112} and {123} planes, the normalized LSR in the Cr-containing MPEAs is either similar or slightly higher than those in MPEAs without Cr, suggesting that the lattice distortion serves as the primary strengthening effect. In the meantime, the normalized USFE and normalized ideal shear strength positively correlate with the lattice distortion on the {110} and {123} planes, but not on the {112} planes. Taken together, our results suggest that whether the chemical composition or lattice distortion plays a more important role in strengthening differs among different slip planes.

4. Discussion

In this work, the effects of lattice distortion and chemical composition were studied to understand their role on slip resistances in four refractory MPEAs. An increase in strength compared with pure metals has been experimentally studied in several refractory MPEAs (Senkov et al., 2010; Kang et al., 2018; Zhang et al., 2015; Han et al., 2018; Yao et al., 2016a; Waseem et al., 2018). In these studies, the increased strength was attributed to a solid solution strengthening effect or a lattice distortion effect. Both MoNbTaV and MoNbTaW have been examined experimentally. In MoNbTaW, Han et al. (2018) found that the compressive yield strength was 996 MPa at room temperature, while Senkov et al. (2011) determined the value to be 1058 MPa, both of which were polycrystalline materials. In MoNbTaV, Yao et al., (2016b) showed that the compressive yield strength was 1525 MPa. These differ from the result obtained in the current study, where MoNbTaW has a higher LSR than MoNbTaV.

The GSFE and LSR calculations provide similar results in terms of which MPEA may perform better mechanically. Both calculations indicated that the Cr-containing MPEAs are superior to those without Cr. This result is attributed to the lattice distortion effect due to the small atomic size of Cr relative to the other elements. This was shown to be the predominant factor according to the edge dislocations on the {112} and {123} planes, however not on the {110} plane. Increased lattice distortion has previously demonstrated a positive effect on the yield stress or lattice friction stress (Lee et al., 2020; Zhao et al., 2019b; Zhao and Nieh, 2017; Ali et al., 2020). Unlike this study, most previously mentioned studies did not contain all constituent elements of the same crystal structure (BCC or FCC), but rather had a mixed. This may have contributed to the increased lattice mismatch. The current study allowed for the opportunity to compare the two main factors, *i.e.*, chemical compositions or lattice distortion. This was considered by the simple rule of

mixtures, which averaged the values of individual elements. The results showed that the MPEA that had a higher value using the simple rule of mixtures did not always have the higher value based on the alloy potentials. This implies that the lattice distortion is the predominant factor to benefit yield strength in some cases. Both GSFE and LSR calculations also provide insight into the local chemical composition. The variation from a symmetrical curve of the GSFE and large variations of the LSR values demonstrate alterations in the local chemical compositions.

The ideal shear strength was used to understand the preferred slip of the glide plane. The {110} plane obtained the lowest value for all four MPEAs. This indicates that the {110} plane is the most likely slip plane for the glide to occur, which is common of BCC metals. Though the {123} plane had slightly higher values, they were very comparable to those of the {110} plane, suggesting that slip may also occur easily on the {123} plane.

Among the four MPEAs, MoNbTaW had the highest screw-to-edge ratios on its respective plane on the {110} and {123} planes, but the lowest on the {112} plane. This shows that MoNbTaW has the highest degree of anisotropy on the former two planes. The MPEA with the highest lattice distortion, CrMoNbTa, has the highest screw-to-edge ratio on the {112} plane, but the lowest on the {110} plane, among the four MPEAs.

5. Conclusion

In this study, we analyzed four refractory MPEAs by calculating the LSR of edge and screw dislocations on three slip planes. The information provides insight into the preferred plane for a dislocation to glide, as well as the effect of lattice distortion and chemical composition. Two of the four MPEAs contained Cr, which has a small atomic radius relative to the other five BCC elements considered in this study. The MPEAs with higher lattice distortion provided results with a higher USFE, ideal shear strength, and LSR values. However, the same may not be said when the latter three values are normalized by the simple rule of mixtures estimation, suggesting the significance of chemical compositions as a strengthening factor in some cases. In addition, though the two Cr-containing MPEAs had higher results, they also had a higher COV, indicating there is more variation in these MPEAs. The {110} plane obtained the lowest LSR values, while the LSR on {123} planes are comparable. This shows that slip may take place on either the {110} plane or the {123} plane, but is difficult on the {112} plane. The ideal shear strength and LSR are generally positively correlated. We also found that the MPEAs with higher lattice distortion generally have lower slip resistance anisotropy. Our results help understand the strengthening effects in various MPEAs and offer a basis for experimental testing that may be done for comparison.

CRediT authorship contribution statement

Rebecca A. Romero: Investigation, Formal analysis, Writing – original draft, Writing – review & editing. **Shuozhi Xu:** Conceptualization, Investigation, Formal analysis, Writing – original draft, Writing – review & editing. **Wu-Rong Jian:** Investigation, Formal analysis, Writing – review & editing. **Irene J. Beyerlein:** Supervision, Conceptualization, Writing – review & editing. **C.V. Ramana:** Supervision, Writing – review & editing.

Declaration of Competing Interest

The authors declare that they have no known competing financial interests or personal relationships that could have appeared to influence the work reported in this paper.

Acknowledgments

RAR acknowledges the Future Leaders in Advanced Materials (FLAM) program sponsored by the Materials Research Laboratory at UC Santa Barbara. RAR and CVR acknowledge, with pleasure, support from the National Science Foundation with NSF-PREM grant #DMR-1827745. WJ would like to acknowledge funding from the Office of Naval Research under Grant No. N000141712810. IJB gratefully acknowledges support from the Office of Naval Research under contract N00014-21-1-2536. Use was made of computational facilities purchased with funds from the National Science Foundation (CNS1725797) and administered by the Center for Scientific Computing (CSC). The CSC is supported by the California NanoSystems Institute and the Materials Research Science and Engineering Center (MRSEC; NSF DMR 1720256) at UC Santa Barbara.

Appendix. Bond length distributions in four MPEAs

In four MPEAs, distributions of the bond length are calculated and are presented in Fig. A.1. Each distribution is fit to the Gaussian equation,

$$y = y_0 + \left[\frac{A}{w\sqrt{\pi/2}}\right] e^{-2\frac{(x-x_c)^2}{w^2}} \tag{2}$$

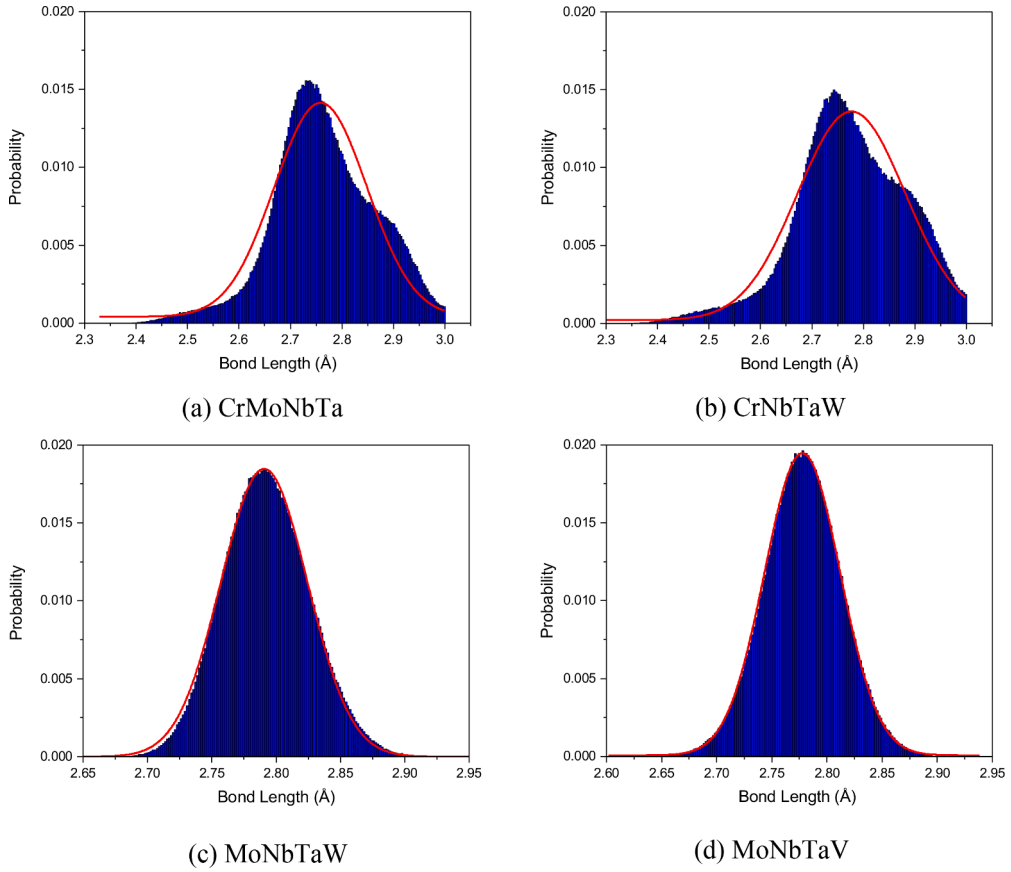

Fig. A.1. The histograms of the bond length distributions for each of the four MPEAs and fitted Gaussian distribution (red curve).

Table A.1
Values of y_0, x_c, w, and A of the bond length distribution in Fig. A.1 for the four MPEAs.

	CrMoNbTa	CrNbTaW	MoNbTaW	MoNbTaV
y_0 (Å)	4.12E-4	2.15E-4	-1.32E-6	7.24E-5
x_c (Å^2)	2.76	2.78	2.79	2.78
w (Å^2)	0.18	0.21	0.067	0.069
A (Å)	0.0031	0.0035	0.0016	0.0017

where x represents the bond length variable, y_0 is the base, x_c is the center of the curve, A is the area under the curve, and w is the full width half maximum. The distribution parameters of the MPEAs are summarized in Table A.1.

References

Aitken, Z.H., Sorkin, V., Zhang, Y.W., 2019. Atomistic modeling of nanoscale plasticity in high-entropy alloys. J. Mater. Res. 34, 1509–1532. https://doi.org/10.1557/jmr.2019.50.

Ali, M.L., Shinzato, S., Wang, V., Shen, Z., Du, J.P., Ogata, S., 2020. An atomistic modeling study of the relationship between critical resolved shear stress and atomic structure distortion in FCC high entropy alloys-relationship in random solid solution and chemical-short-range-order alloys. Mater. Trans. 61, 605. https://doi.org/10.2320/matertrans.MT-MK2019007.

Antillon, E., Woodward, C., Rao, S.I., Akdim, B., 2021. Chemical short range order strengthening in BCC complex concentrated alloys. Acta Mater. 215, 117012 https://doi.org/10.1016/j.actamat.2021.117012.

Byggmästar, J., Nordlund, K., Djurabekova, F., 2021. Modeling refractory high-entropy alloys with efficient machine-learned interatomic potentials: defects and segregation. Phys. Rev. B 104, 104101. https://doi.org/10.1103/PhysRevB.104.104101.

Cantor, B., Chang, I.T.H., Knight, P., Vincent, A.J.B., 2004. Microstructural development in equiatomic multicomponent alloys. Mater. Sci. Eng. A 375–377, 213–218. https://doi.org/10.1016/j.msea.2003.10.257.

Chan, K.S., 2004. Cyclic oxidation response of multiphase niobium-based alloys. Metall. Mater. Trans. A 35, 589–597. https://doi.org/10.1007/s11661-004-0370-7.

Chen, B., Li, S., Zong, H., Ding, X., Sun, J., Ma, E., 2020. Unusual activated processes controlling dislocation motion in body-centered-cubic high-entropy alloys. Proc. Natl. Acad. Sci. U. S. A. 117, 16199–16206. https://doi.org/10.1073/pnas.1919136117.
Couzinié, J.P., Senkov, O.N., Miracle, D.B., Dirras, G., 2018. Comprehensive data compilation on the mechanical properties of refractory high-entropy alloys. Data Br. 21, 1622–1641. https://doi.org/10.1016/j.dib.2018.10.071.
Fang, Q., Chen, Y., Li, J., Jiang, C., Liu, B., Liu, Y., Liaw, P.K., 2019. Probing the phase transformation and dislocation evolution in dual-phase high-entropy alloys. Int. J. Plast. 114, 161–173. https://doi.org/10.1016/j.ijplas.2018.10.014.
George, E.P., Raabe, D., Ritchie, R.O., 2019. High-entropy alloys. Nat. Rev. Mater. 4, 515–534. https://doi.org/10.1038/s41578-019-0121-4.
Ghafarollahi, A., Maresca, F., Curtin, W.A., 2019. Solute/screw dislocation interaction energy parameter for strengthening in bcc dilute to high entropy alloys. Model. Simul. Mater. Sci. Eng. 27, 085011 https://doi.org/10.1088/1361-651X/ab4969.
Gorr, B., Mueller, F., Christ, H.J., Mueller, T., Chen, H., Kauffmann, A., Heilmaier, M., 2016. High temperature oxidation behavior of an equimolar refractory metal-based alloy 20Nb-20Mo-20Cr-20Ti-20Al with and without Si addition. J. Alloy. Compd. 688, 468–477. https://doi.org/10.1016/j.jallcom.2016.07.219.
Han, Z.D., Luan, H.W., Liu, X., Chen, N., Li, X.Y., Shao, Y., Yao, K.F., 2018. Microstructures and mechanical properties of TixNbMoTaW refractory high-entropy alloys. Mater. Sci. Eng. A 712, 380–385. https://doi.org/10.1016/j.msea.2017.12.004.
Hua, D., Xia, Q., Wang, W., Zhou, Q., Li, S., Qian, D., Shi, J., Wang, H., 2021. Atomistic insights into the deformation mechanism of a CoCrNi medium entropy alloy under nanoindentation. Int. J. Plast. 142, 102997 https://doi.org/10.1016/j.ijplas.2021.102997.
Huang, R., Zhang, Q., Zhang, X., Li, J., Cao, T., Yao, J., Xue, Y., Gao, H., Li, X., 2021. Dynamic recrystallization-induced temperature insensitivity of yield stress in single-crystal $Al_{1.2}$ CrFeCoNi micropillars. Sci. China Tech. Sci. 64, 11–22. https://doi.org/10.1007/s11431-020-1660-8.
Hull, D., Bacon, D.J., 2011. Introduction to Dislocations, 5th ed. Elsevier.
Johnson, R.A., 1989. Alloy models with the embedded-atom method. Phys. Rev. B 39, 12554–12559. https://doi.org/10.1103/PhysRevB.39.12554.
Kang, B., Lee, J., Ryu, H.J., Hong, S.H., 2018. Ultra-high strength WNbMoTaV high-entropy alloys with fine grain structure fabricated by powder metallurgical process. Mater. Sci. Eng. A 712, 616–624. https://doi.org/10.1016/j.msea.2017.12.021.
Kim, I.H., Oh, H.S., Lee, K.S., Park, E.S., 2021a. Optimization of conflicting properties via engineering compositional complexity in refractory high entropy alloys. Scr. Mater. 199, 113839 https://doi.org/10.1016/j.scriptamat.2021.113839.
Kim, I.H., Oh, H.S., Kim, S.J., Park, E.S., 2021b. Rapid assessment of solid solution hardening via atomic size misfit parameter in refractory concentrated alloys. J. Alloy. Compd. 886, 161320 https://doi.org/10.1016/j.jallcom.2021.161320.
Kumar, A., Kedjar, B., Su, Y., Thilly, L., Beyerlein, I.J., 2020. Atomic-level calculations and experimental study of dislocations in InSb. J. Appl. Phys. 127, 135104 https://doi.org/10.1063/1.5139285.
Lee, C., Chou, Y., Kim, G., Gao, M.C., An, K., Brechtl, J., Zhang, C., Chen, W., Poplawsky, J.D., Song, G., Ren, Y., Chou, Y.C., Liaw, P.K., 2020. Lattice-distortion-enhanced yield strength in a refractory high-entropy alloy. Adv. Mater. 32, 2004029 https://doi.org/10.1002/adma.202004029.
Li, J., Chen, H., Fang, Q., Jiang, C., Liu, Y., Liaw, P.K., 2020c. Unraveling the dislocation-precipitate interactions in high-entropy alloys. Int. J. Plast. 133, 102819 https://doi.org/10.1016/j.ijplas.2020.102819.
Li, L., Fang, Q., Li, J., Liu, B., Liu, Y., Liaw, P.K., 2020b. Lattice-distortion dependent yield strength in high entropy alloys. Mater. Sci. Eng. A 784, 139323. https://doi.org/10.1016/j.msea.2020.139323.
Li, X.G., Chen, C., Zheng, H., Zuo, Y., Ong, S.P., 2020a. Complex strengthening mechanisms in the NbMoTaW multi-principal element alloy. npj Comput. Mater. 6, 70. https://doi.org/10.1038/s41524-020-0339-0.
Lim, H., Weinberger, C.R., Battaile, C.C., Buchheit, T.E., 2013. Application of generalized non-schmid yield law to low-temperature plasticity in bcc transition metals. Model. Simul. Mater. Sci. Eng. 21, 045015 https://doi.org/10.1088/0965-0393/21/4/045015.
Lin, D.Y., Wang, S.S., Peng, D.L., Li, M., Hui, X.D., 2013. An *n*-body potential for a Zr-Nb system based on the embedded-atom-method. J. Phys. Condens. Matter 25, 105404. https://doi.org/10.1088/0953-8984/25/10/105404.
Lin, Z., Johnson, R.A., Zhigilei, L.V., 2008. Computational study of the generation of crystal defects in a bcc metal target irradiated by short laser pulses. Phys. Rev. B. 77, 214108 https://doi.org/10.1103/PhysRevB.77.214108.
Liu, S., Wei, Y., 2017. The Gaussian distribution of lattice size and atomic level heterogeneity in high entropy alloys. Extrem Mech. Lett. 11, 84–88. https://doi.org/10.1016/j.eml.2016.10.007.
Liu, X., Pei, Z., Eisenbach, M., 2019. Dislocation core structures and Peierls stresses of the high-entropy alloy NiCoFeCrMn and its subsystems. Mater. Des. 180, 107955 https://doi.org/10.1016/j.matdes.2019.107955.
Lo, K.C., Chang, Y.J., Murakami, H., Yeh, J.W., Yeh, A.C., 2019. An oxidation resistant refractory high entropy alloy protected by $CrTaO_4$-based oxide. Sci. Rep. 9, 7266. https://doi.org/10.1038/s41598-019-43819-x.
Maresca, F., Curtin, W.A., 2020. Mechanistic origin of high strength in refractory BCC high entropy alloys up to 1900K. Acta Mater. 182, 235–249. https://doi.org/10.1016/j.actamat.2019.10.015.
Mayahi, R., 2020. An investigation concerning generalized stacking fault behavior of AlCo*x*CrFeNi ($0.25 \leq x \leq 2$) high entropy alloys: Insights from first-principles study. J. Alloy. Compd. 818, 152928 https://doi.org/10.1016/j.jallcom.2019.152928.
Mishra, S., Maiti, S., Rai, B., 2021. Computational property predictions of Ta–Nb–Hf–Zr high-entropy alloys. Sci. Rep. 11, 4815. https://doi.org/10.1038/s41598-021-84260-3.
Mitchell, T.E., 1968. Slip in body-centred cubic crystals. Philos. Mag. 17, 1169–1194. https://doi.org/10.1080/14786436808223194.
Oh, H.S., Odbadrakh, K., Ikeda, Y., Mu, S., Körmann, F., Sun, C.J., Ahn, H.S., Yoon, K.N., Ma, D., Tasan, C.C., Egami, T., Park, E.S., 2021. Element-resolved local lattice distortion in complex concentrated alloys: an observable signature of electronic effects. Acta Mater. 216, 117135 https://doi.org/10.1016/j.actamat.2021.117135.
Pei, Z., 2018. An overview of modeling the stacking faults in lightweight and high-entropy alloys: theory and application. Mater. Sci. Eng. A 737, 132–150. https://doi.org/10.1016/j.msea.2018.09.028.
Plimpton, S., 1995. Fast parallel algorithms for short-range molecular dynamics. J. Comput. Phys. 117, 1–19. https://doi.org/10.1006/jcph.1995.1039.
Roy, A., Sreeramagiri, P., Babuska, T., Krick, B., Ray, P.K., Balasubramanian, G., 2021. Lattice distortion as an estimator of solid solution strengthening in high-entropy alloys. Mater. Charact. 172, 110877 https://doi.org/10.1016/j.matchar.2021.110877.
Senkov, O.N., Wilks, G.B., Miracle, D.B., Chuang, C.P., Liaw, P.K., 2010. Refractory high-entropy alloys. Intermetallics 18, 1758–1765. https://doi.org/10.1016/j.intermet.2010.05.014.
Senkov, O.N., Wilks, G.B., Scott, J.M., Miracle, D.B., 2011. Mechanical properties of $Nb_{25}Mo_{25}Ta_{25}W_{25}$ and $V_{20}Nb_{20}Mo_{20}Ta_{20}W_{20}$ refractory high entropy alloys. Intermetallics 19, 698–706. https://doi.org/10.1016/j.intermet.2011.01.004.
Senkov, O.N., Miracle, D.B., Chaput, K.J., Couzinie, J.P., 2018. Development and exploration of refractory high entropy alloys - A review. J. Mater. Res. 33, 3092–3128. https://doi.org/10.1557/jmr.2018.153.
Smith, L.T.W., Su, Y., Xu, S., Hunter, A., Beyerlein, I.J., 2020. The effect of local chemical ordering on Frank-Read source activation in a refractory multi-principal element alloy. Int. J. Plast. 134, 102850 https://doi.org/10.1016/j.ijplas.2020.102850.
Song, H., Tian, F., Hu, Q.M., Vitos, L., Wang, Y., Shen, J., Chen, N., 2017. Local lattice distortion in high-entropy alloys. Phys. Rev. Mater. 1, 023404 https://doi.org/10.1103/PhysRevMaterials.1.023404.
Srivastava, K., Gröger, R., Weygand, D., Gumbsch, P., 2013. Dislocation motion in tungsten: atomistic input to discrete dislocation simulations. Int. J. Plast. 47, 126–142. https://doi.org/10.1016/j.ijplas.2013.01.014.
Su, Y., Xu, S., Beyerlein, I.J., 2019. Density functional theory calculations of generalized stacking fault energy surfaces for eight face-centered cubic transition metals. J. Appl. Phys. 126, 105112 https://doi.org/10.1063/1.5115282.
Van De Walle, A., Tiwary, P., De Jong, M., Olmsted, D.L., Asta, M., Dick, A., Shin, D., Wang, Y., Chen, L.Q., Liu, Z.K., 2013. Efficient stochastic generation of special quasirandom structures. Calphad 42, 13–18. https://doi.org/10.1016/j.calphad.2013.06.006.

Varvenne, C., Luque, A., Nöhring, W.G., Curtin, W.A., 2016. Average-atom interatomic potential for random alloys. Phys. Rev. B 93, 104201. https://doi.org/10.1103/PhysRevB.93.104201.
Vitek, V., 2011. Atomic level computer modelling of crystal defects with emphasis on dislocations: past, present and future. Prog. Mater. Sci. 56, 577–585. https://doi.org/10.1016/j.pmatsci.2011.01.002.
Vitek, V., 1992. Structure of dislocation cores in metallic materials and its impact on their plastic behaviour. Prog. Mater. Sci. 36, 1–27. https://doi.org/10.1016/0079-6425(92)90003-P.
Wadsworth, J., Nieh, T.G., Stephens, J.J., 1988. Recent advances in aerospace refractory metal alloys. Int. Mater. Rev. 33, 131–150. https://doi.org/10.1179/imr.1988.33.1.131.
Wang, F., Balbus, G.H., Xu, S., Su, Y., Shin, J., Rottmann, P.F., Knipling, K.E., Stinville, J.C., Mills, L.H., Senkov, O.N., Beyerlein, I.J., Pollock, T.M., Gianola, D.S., 2020. Multiplicity of dislocation pathways in a refractory multiprincipal element alloy. Science 370, 95–101. https://doi.org/10.1126/science.aba3722.
Wang, X., Xu, S., Jian, W.R., Li, X.G., Su, Y., Beyerlein, I.J., 2021. Generalized stacking fault energies and Peierls stresses in refractory body-centered cubic metals from machine learning-based interatomic potentials. Comput. Mater. Sci. 192, 110364 https://doi.org/10.1016/j.commatsci.2021.110364.
Warlimont, H., Martienssen, W., 2018. Springer Handbook of Materials Data. Springer.
Waseem, O.A., Lee, J., Lee, H.M., Ryu, H.J., 2018. The effect of Ti on the sintering and mechanical properties of refractory high-entropy alloy Ti*x*WTaVCr fabricated via spark plasma sintering for fusion plasma-facing materials. Mater. Chem. Phys. 210, 87–94. https://doi.org/10.1016/j.matchemphys.2017.06.054.
Xiao, Y., Kuang, W., Xu, Y., Wu, L., Gong, W., Qian, J., Zhang, Q., He, Y., 2019. Microstructure and oxidation behavior of the CrMoNbTaV high-entropy alloy. J. Mater. Res. 34, 301–308. https://doi.org/10.1557/jmr.2018.340.
Xu, S., Hwang, E., Jian, W.R., Su, Y., Beyerlein, I.J., 2020a. Atomistic calculations of the generalized stacking fault energies in two refractory multi-principal element alloys. Intermetallics 124, 106844. https://doi.org/10.1016/j.intermet.2020.106844.
Xu, S., Su, Y., Smith, L.T.W., Beyerlein, I.J., 2020b. Frank-read source operation in six body-centered cubic refractory metals. J. Mech. Phys. Solids 141, 104017. https://doi.org/10.1016/j.jmps.2020.104017.
Xu, S., Su, Y., Jian, W.R., Beyerlein, I.J., 2021. Local slip resistances in equal-molar MoNbTi multi-principal element alloy. Acta Mater. 202, 68–79. https://doi.org/10.1016/j.actamat.2020.10.042.
Xu, S., Chavoshi, S.Z., Su, Y., 2022. On calculations of basic structural parameters in multi-principal element alloys using small atomistic models. Comput. Mater. Sci. 202, 110942 https://doi.org/10.1016/j.commatsci.2021.110942.
Yao, H., Qiao, J.W., Gao, M.C., Hawk, J.A., Ma, S.G., Zhou, H., 2016b. MoNbTaV medium-entropy alloy. Entropy 18, 189. https://doi.org/10.3390/e18050189.
Yao, H.W., Qiao, J.W., Gao, M.C., Hawk, J.A., Ma, S.G., Zhou, H.F., Zhang, Y., 2016a. NbTaV-(Ti,W) refractory high-entropy alloys: experiments and modeling. Mater. Sci. Eng. A 674, 203–211. https://doi.org/10.1016/j.msea.2016.07.102.
Yeh, J.W., 2015. Physical metallurgy of high-entropy alloys. JOM 67, 2254–2261. https://doi.org/10.1007/s11837-015-1583-5.
Yeh, J.W., Chen, S.K., Lin, S.J., Gan, J.Y., Chin, T.S., Shun, T.T., Tsau, C.H., Chang, S.Y., 2004. Nanostructured high-entropy alloys with multiple principal elements: novel alloy design concepts and outcomes. Adv. Eng. Mater. 6, 299–303. https://doi.org/10.1002/adem.200300567.
Yin, S., Zuo, Y., Abu-Odeh, A., Zheng, H., Li, X.G., Ding, J., Ong, S.P., Asta, M., Ritchie, R.O., 2021. Atomistic simulations of dislocation mobility in refractory high-entropy alloys and the effect of chemical short-range order. Nat. Commun. 12, 4873. https://doi.org/10.1038/s41467-021-25134-0.
Zhang, B., Gao, M.C., Zhang, Y., Guo, S.M., 2015. Senary refractory high-entropy alloy CrxMoNbTaVW. Calphad 51, 193–201. https://doi.org/10.1016/j.calphad.2015.09.007.
Zhang, Q., Huang, R., Zhang, X., Cao, T., Xue, Y., Li, X., 2021. Deformation mechanisms and remarkable strain hardening in single-crystalline high-entropy-alloy micropillars/nanopillars. Nano Lett. 21, 3671–3679. https://doi.org/10.1021/acs.nanolett.1c00444.
Zhao, S., Osetsky, Y., Stocks, G.M., Zhang, Y., 2019a. Local-environment dependence of stacking fault energies in concentrated solid-solution alloys. npj Comput. Mater. 5, 13. https://doi.org/10.1038/s41524-019-0150-y.
Zhao, L., Zong, H., Ding, X., Lookman, T., 2021. Anomalous dislocation core structure in shock compressed bcc high-entropy alloys. Acta Mater. 209, 116801 https://doi.org/10.1016/j.actamat.2021.116801.
Zhao, Y.Y., Lei, Z.F., Lu, Z.P., Huang, J.C., Nieh, T.G., 2019b. A simplified model connecting lattice distortion with friction stress of Nb-based equiatomic high-entropy alloys. Mater. Res. Lett. 7, 340–346. https://doi.org/10.1080/21663831.2019.1610105.
Zhao, Y.Y., Nieh, T.G., 2017. Correlation between lattice distortion and friction stress in Ni-based equiatomic alloys. Intermetallics 86, 45–50. https://doi.org/10.1016/j.intermet.2017.03.011.
Zuo, Y., Chen, C., Li, X., Deng, Z., Chen, Y., Behler, J., Csányi, G., Shapeev, A.V., Thompson, A.P., Wood, M.A., Ong, S.P., 2020. Performance and cost assessment of machine learning interatomic potentials. J. Phys. Chem. A 124, 731–745. https://doi.org/10.1021/acs.jpca.9b08723.
Zhou, S.J., Carlsson, A.E., Thomson, R., 1994. Dislocation core-core interaction and Peierls stress in a model hexagonal lattice. Phys. Rev. B 49, 6451. https://doi.org/10.1103/PhysRevB.49.6451.
Zhou, X.W., Johnson, R.A., Wadley, H.N.G., 2004. Misfit-energy-increasing dislocations in vapor-deposited CoFe/NiFe multilayers. Phys. Rev. B 69, 144113. https://doi.org/10.1103/PhysRevB.69.144113.
Zhou, X.W., Wadley, H.N.G., Johnson, R.A., Larson, D.J., Tabat, N., Cerezo, A., Petford-Long, A.K., Smith, G.D.W., Clifton, P.H., Martens, R.L., Kelly, T.F., 2001. Atomic scale structure of sputtered metal multilayers. Acta Mater. 49, 4005–4015. https://doi.org/10.1016/S1359-6454(01)00287-7.
Zunger, A., Wei, S.H., Ferreira, L.G., Bernard, J.E., 1990. Special quasirandom structures. Phys. Rev. Lett. 65, 353–356. https://doi.org/10.1103/PhysRevLett.65.353.